Editors' Suggestion

Decoherence in a ballistic quantum interferometer due to the interplay of radio-frequency electromagnetic field and surface acoustic wave

Shung-Kang Koh,[1] Ching-Ping Lee,[1] Tzu-Kan Hsiao,[1] Io-Chun Hoi,[2] Yen-Hsiang Lin,[1] Chung-Yu Mou,[1] Dah-Chin Ling,[3] Yung-Fu Chen,[4] Cen-Shawn Wu,[5] and Jeng-Chung Chen[1,*]

[1]Department of Physics, National Tsing Hua University, Hsinchu 30013, Taiwan
[2]Department of Physics, City University of Hong Kong, Tat Chee Avenue, Kowloon 999077, Hong Kong SAR
[3]Department of Physics, Tamkang University, Tamsui Dist., New Taipei City 25137, Taiwan
[4]Department of Physics, National Central University, Jhongli 32001, Taiwan
[5]Department of Physics, National Changhua University of Education, Changhua 50007, Taiwan

(Received 17 November 2023; revised 27 December 2024; accepted 7 January 2025; published 22 January 2025)

We report on studies of the decoherence processes of a ballistic quantum interferometer subjected to a radio-frequency (RF) electromagnetic (EM) field and a surface acoustic wave (SAW). The device consists of an Aharonov-Bohm (AB) ring sandwiched between two interdigital transducers (IDTs), where the AB ring serves as a phase sensor and the IDTs function as a controlled source of environmental noise. By employing the IDTs with an RF-EM field to launch a SAW train through the ring, we extract the decoherence rate Γ_ϕ from the AB oscillation amplitude and investigate the dephasing process through the RF power $P_{\rm rf}$ dependence of Γ_ϕ, the electronic temperature T_s, and acoustoelectric current $I_{\rm ae}$ spectrum. Our data reveal that the bandwidth-narrowing feature caused by Bragg reflections of the SAW is consistently found in the spectra of Γ_0, T_s, and $I_{\rm ae}$, suggesting that the piezoelectric field is the dominant EM field contributing to decoherence. At the resonance frequency, the decoherence rate follows $P_{\rm rf}^{1/5}$ dependence due to thermal fluctuation of the alternating electric current by the EM field. At the off-resonance condition, we identify that the asymmetric Γ_0 spectrum is induced by the crosstalk of SAW interference under the influence of a weak $P_{\rm rf}$. Furthermore, we find the optimal conditions for operating the SAW to minimize dephasing without thermal heating. The underlying mechanism responsible for the decoherence is attributed to the enhancement of charge-charge interactions in the presence of the EM field and the SAW. These findings are crucial for the development of quantum electronic devices leveraging SAW technology.

DOI: 10.1103/PhysRevB.111.045150

I. INTRODUCTION

Understanding the decoherence mechanism lies in the central theme of the development of quantum technologies [1–3]. Decoherence arises from the interaction of a quantum system with its surrounding environment, with the noise spectrum characterizing the frequency dependence of environmental disturbances, including temperature fluctuations, electromagnetic (EM) interference, and unwanted interactions in the experimental setup. In general, the decoherence rate Γ_ϕ of a quantum system is intimately related to the noise power spectral density $S_i(f)$ of the coupled noise fluctuations, where the index i stands for a specific decay source, and f represents frequency. For example, the decoherence rate of a quantum ballistic interferometer can be expressed as $\Gamma_\phi = (e^2/2\hbar^2)S_{ee}(f)$ in the spin-degenerate and single-channel limit [4], where $S_{ee}(f)$ is primarily attributed to the external charge fluctuations, which are proportional to the electronic temperature T_e in the vicinity of the electron path [5]. However, thermal (or Nyquist) noise-induced decoherence (denoted as $S_{\rm th}$) is coincidentally proportional to the lattice temperature T_L. Therefore, it has been a challenging issue to distinguish between the environmental thermal- and electron-heating effects in Γ_ϕ [6–8]. Alternatively, extrinsic environmental EM field-induced thermal fluctuations in the alternative electric current, known as EM noise with noise spectrum $S_{\rm ac}(f)$, is believed to be a leading dephasing source in mesoscopic systems [9,10]. To date, high-frequency decoherence mechanisms have been thoroughly investigated in diffusive quantum systems [11,12], whereas corresponding studies in ballistic quantum systems, a prerequisite platform for fabricating quantum electronic devices, remain unexplored.

The intersection of mechanical phonons and quantum informatics has recently been at the forefront of quantum technology research [13,14]. For instance, the implementation of flying qubits within quantum ballistic electronics, where electrons residing in quantum dots or single-electron channels are shuttled under temporal-controlled surface acoustic waves (SAWs), presents an effective technique for transmitting quantum information [15–21]. However, this scheme could be intriguing because quantum states carried by the moving electrons could be fragile against the SAW-modulated confinement potential. Conceptually, a SAW can be viewed as surrounding noise, characterized by a noise spectrum

*Contact author: jcchen@phys.nthu.edu.tw

$S_{\mathrm{SAW}}(f)$, that may lead to the loss of quantum phase coherence [4,6–8]. This raises essential questions about how the EM field associated with the SAW propagation influences the phase coherence of the shuttled electrons [9–12]. Furthermore, the radio-frequency (RF)-EM field used to excite the SAW is mediated by the SAW throughout the device; consequently, how these various perturbations affect the phase coherence inherent to the electrons needs to be clarified. Here, we employ a ballistic quantum interferometer, an Aharonov-Bohm (AB) ring fabricated in a GaAs/AlGaAs heterostructure, and take advantage of the shallow electric potential modulation on a piezoelectric substrate to generate the SAW using an interdigital transducer (IDT). The phase information is obtained by the AB phase, accumulated with circulating electrons.

II. DISCUSSION

The optical image of our device is displayed in Fig. 1(a). The device consists of two ballistic AB rings defined on the two-dimensional electron gas (2DEG) of a GaAs/AlGaAs heterostructure and embedded between a pair of IDT, denoted as IDT1 and IDT2. To minimize scattering, crosstalk, and attenuation of the SAW, we etch away the 2DEG outside the interferometer so there are no Schottky gates between the IDTs. In this paper, we aim to investigate the variation of Γ_ϕ under the influences of the RF-EM field, SAW, and SAW-induced acoustoelectric current I_{ae} in a multichannel ballistic quantum system and unveil the interplay of Γ_ϕ with $S_{\mathrm{ac}}(f)$, $S_{\mathrm{SAW}}(f)$, and S_{th}. We identify the charge-charge interaction as the dominant decoherence source. The scanning electron microscope (SEM) image of the device is shown on the left side of Fig. 1(a). The relevant properties of the patterned 2DEG are listed as follows: depth 90 nm, mobility $\mu = 2.2 \times 10^5\ \mathrm{cm^2/Vs}$, and carrier density $n_s = 3.3 \times 10^{11}\ \mathrm{cm^{-2}}$ measured at liquid He temperature, corresponding to an elastic mean free path $\ell_e \sim 1.6\ \mu\mathrm{m}$. The ring structure is laterally confined by a wet etch with an etching depth of ~100 nm, which completely removes the doped layer to minimize the attenuation of the SAW. Details of the device fabrication are described elsewhere [6]. The average diameter of the ring is ~1.84 μm with a linewidth of 550 nm. The interferometer employed consists of ~8 ballistic channels. Each IDT made by Cr/Au layers consists of 25 pairs of interleaved fingers with 700 μm length, 4 μm width, and 4 μm in spacing, corresponding to a periodicity of the fingers $\lambda_{\mathrm{IDT}} \sim 16\ \mu\mathrm{m}$. The width of the wavefront of the SAW beam is determined by the aperture of the fingers ~650 μm. The SAW induced by the IDT propagates a distance of 220 μm before reaching the ring. The IDT is parallel to the direction of the transport channel of the ring, as shown in Fig. 1(a). The contact leads L_1 and L_2 are employed to measure V_{xx}, whereas leads L_2 and L_H are used to measure the Hall voltage, and lead L_E is not used. Note that the pair of leads L_1 and L_2 is also utilized to measure I_{ae}. The rectangular structure connected to the extended leads represents the etching mesa after defining the ring pattern. The device layout, with a transducer at either end of the interferometer, is designed to use the second transducer to detect

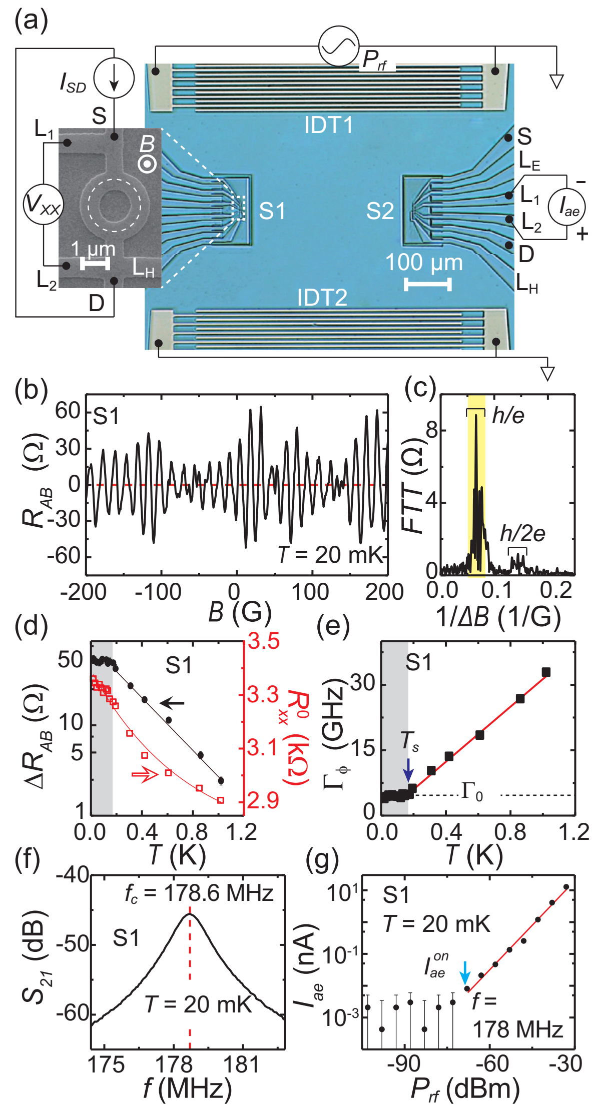

FIG. 1. (a) Optical micrograph of the device and the experimental setup diagram. The device includes two interdigital transducers (IDTs) for converting electrical signals to surface acoustic waves (SAWs) and vice versa and two Aharonov-Bohm (AB) interferometers employed as phase sensors under the SAW. The scanning electron microscope (SEM) image of the enlarged ring structure is shown in the left corner. (b) AB oscillation of the magnetoresistance R_{AB} of ring 1, labeled S1, after subtracting the background signal $R_{xx}(B)$, defined as V_{xx}/I_{SD}. Data are taken without SAW perturbations. (c) Fast Fourier transform (FFT) of R_{AB} is used to determine the amplitude ΔR_{AB} of the AB oscillations. (d) ΔR_{AB} (black circle) and the background resistance R^0_{xx}, defined as $R_{xx}(0)$ (red square) vs temperature T. The black solid line is an exponential fit of data discussed in the main text. (e) Decoherence rate Γ_ϕ as a function of T, extracted from the data presented in (d), where the saturation temperature $T_s \sim 190$ mK and decoherence rate $\Gamma_0 = 3.9$ GHz. The red solid line is fit by bT/τ_L, with b obtained from (d), which is only valid for $T > 190$ mK. (f) Transmission coefficient S_{21} of the IDTs as a function of frequency f with a central frequency $f_c = 178.6$ MHz. (g) Acoustoelectric current I_{ae} vs the radio-frequency (RF) power applied P_{rf} on IDT1, while IDT2 remains inactive and grounded.

the transmission of the SAW, providing information on the attenuation and an experimental checkout in acoustoelectric current measurements.

Four devices with identical designs have been measured and exhibit consistent results. Here, we present data obtained from two of them, S1 and S2. The device is cooled in a ^{3}H/^{4}H dilution refrigerator with a base temperature of 20 mK. A schematic diagram of the electric measurement is displayed in Fig. 1(a). We measure the four-terminal electric resistance R_{xx} of the device with an excitation current $I_{SD} \leqslant 10$ nA at 17 Hz.

Figure 1(b) shows R_{AB} as a function of magnetic field after subtracting a slowly varying background $R_{xx}(B) = dV_{xx}/dI_{SD}$ of $\sim$3.4 kΩ (see Ref. [7] for the procedures), while both IDTs are unfed. We find that R_{AB} exhibits AB oscillations with a period of 15 ± 7 G, in agreement with the period of $B = h/eA$, where h/e is flux quantum Φ_0, and $A = 2.7 \pm 1.0\,\mu\text{m}^2$ is the enclosed area of the ring. To quantify the degree of coherence, we show the fast Fourier transform (FFT) of R_{AB} in Fig. 1(c). The amplitudes of the AB oscillations ΔR_{AB} are estimated by integrating the spectra over the width of the h/e peak [8]. Figure 1(d) shows the temperature (T) dependence of ΔR_{AB} and $R_{xx}(0)$, defined as R^0_{xx}. The oscillation amplitude saturates for $T \sim <190$ mK and then decreases with increasing T. It is generally believed that the saturation of ΔR_{AB} is due to the saturation of Γ_ϕ. Such saturation has been previously observed in various systems; however, its origin remains unclear [22,23]. For $T > 190$ mK, we can fit ΔR_{AB} with an exponential decay function of temperature: $\Delta R_{AB} \propto \exp(-bT)$, where $b \sim 3.44\,\text{K}^{-1}$ is the fitting parameter and signifies the damping rate of the AB amplitude with T [8].

Now we describe the procedure for extracting Γ_ϕ. First, we define ΔR^{max}_{AB} as the maximum AB amplitude ΔR_{AB} measured at the base temperature and extracted from the FFT. Empirically, the attenuation of the AB oscillations due to phase-breaking can be expressed as

$$\Gamma_\phi = \tau_L^{-1} \ln\left(\frac{\Delta R^{max}_{AB}}{\Delta R_{AB}}\right) + \Gamma_0, \qquad (1)$$

where $\tau_L^{-1} = v_F/L$ is the transit rate of electrons through a ring arm of length $L \sim 2.89\,\mu$m, and v_F is the Fermi velocity, estimated to be $\sim 2.4 \times 10^5$ m/s [6–8]. We define $\Gamma_0 = \Gamma_\phi$ at the saturation temperature $T_s \sim 190$ mK, where Γ_0 is viewed as the intrinsic decoherence rate of the device studied [22]. We consider for $T < T_s$, $\Gamma_0 \sim \Gamma_\phi$. The red line shown in Fig. 1(e) is a linear fit of $\Gamma_\phi(T)$ with a slope of $b/\tau_L = 32.8$ GHz/K in the temperature range from 190 mK to 1.05 K. The error bars of Γ_ϕ are estimated from the corresponding FFT background. Since the slope is sample dependent, we estimate $\Gamma_0 \sim k_B T_s/h \sim 3.9$ GHz based on the thermal averaging effect [4], which fairly fall within the values evaluated by bT/τ_L.

As displayed in Fig. 1(d), R^0_{xx} slightly increases with decreasing T. This feature is likely associated with the nature of the phonon-assisted hopping process and boundary-induced scattering often observed in quasi-one-dimensional wire [24,25]. We will utilize the variation of R^0_{xx} with T as a thermometer to estimate the electronic temperature T_e of the device [26,27]. To demonstrate the functionality of IDT1 and IDT2, we measure the transmission coefficient S_{21} with a vector network analyzer, as shown in Fig. 1(f). The IDTs, behaving as a SAW band-pass filter, effectively generate and detect a SAW with a central frequency of $f_c = 178.6$ MHz, consistent with $f_c \sim v_{SAW}/\lambda_{IDT}$, where v_{SAW} is $\sim$2900 m/s in GaAs [28]. The bandwidth of the f_c resonance peak is $\sim$1.5 MHz. Theoretically, for a single-electrode IDT adopted in our experiment, the bandwidth can be evaluated by the equation $\delta f_{21} = f_c/N \sim 7.1$ MHz, where $N = 25$ is the number of finger pairs [29], which is significantly larger than the observed value of 1.5 MHz. The bandwidth-narrowing feature is attributed to the Bragg reflection of SAW from IDT2 with a periodic metal strip [29]. The P_{rf} dependence of the acoustoelectric current I_{ae} is shown in Fig. 1(g). Note that the noise floor of I_{ae} is $\sim$10 pA in our experiment, and a discernible I_{ae} is measured around $P_{rf} \geqslant -67$ dBm. The RF source feeding to the IDT1 is pulse modulated at frequency $\sim$1 kHz with a duty cycle of 0.5. An ammeter is connected to two ohmic contacts on the 2DEG mesa, and I_{ae} is measured by a standard lock-in technique with details described in an earlier report [30]. The onset of acoustoelectric current is denoted as I^{on}_{ae} above which I_{ae} linearly increases with increasing P_{rf} : $I_{ae} = 0.0255\,(\text{A/W}) \times P_{rf}$. The line loss, ~ -10 dB at 4.2 K, has been accounted for P_{rf}. We stress that the magnitude of P_{rf} shown in the measurement of I_{ae} has been calibrated to that in the measurement of AB oscillations under a continuous RF drive.

We apply a continuous RF field on IDT1, keep IDT2 unfed and grounded, and measure the AB oscillations. To minimize the external dephasing that may be sensed by the interference of the measurement setup, R_{AB} and I_{ae} are separately measured using the schemes mentioned above. Figure 2(a) shows selected R_{AB} traces of S1 as a function of applied magnetic field B under various power levels at the central frequency f_c. The trace of AB oscillations remains an unperturbed value under a weak excitation ($P_{rf} \leqslant -60$ dBm) and gradually attenuates with increasing P_{rf}, eventually diminishing at $P_{rf} \geqslant -30$ dBm. Furthermore, we observe additional weak fluctuations superimposed on the AB oscillations, which causes a wider error bar in extracting ΔR_{AB}. The corresponding uncertainty $\Delta\Gamma_\phi$ is estimated to be $\sim$1.0 GHz, which sets the minimum phase resolution of the interferometer. The enhanced noises could be reconciled by the reflection of a small fraction of the SAW beam from the second transducer and the interference between the forward and backward SAW beams.

Figures 2(b) and 2(d) show R^0_{xx} and Γ_ϕ as a function of frequency under different RF power levels applied on IDT1. We substitute ΔR_{AB}, measured under various SAW power and frequency values, into Eq. (1), where ΔR^{max}_{AB} is obtained at the base temperature of 20 mK. With these procedures, we can extract Γ_ϕ by using Eq. (1). Meanwhile we can estimate the electronic temperature T_e from the value of R^0_{xx} by the temperature dependence of $R^0_{xx}(T)$, as shown in Fig. 1(d). The monotonic decrease in R^0_{xx} with increasing P_{rf} suggests a heating effect induced by a continuous RF-field drive. Accordingly, Γ_ϕ increases with P_{rf}, consistent with a decrease of R^0_{xx}, which indicates the increasing of the electronic temperature T_e of the device. To quantify the variation of T_e with f and P_{rf}, we present a color plot of the electronic temperature $T_e(f, P_{rf})$ extracted from $R^0_{xx}(T)$ in Fig. 2(c). The white dashed line in Fig. 2(c) is an isothermal line of T_s above which the

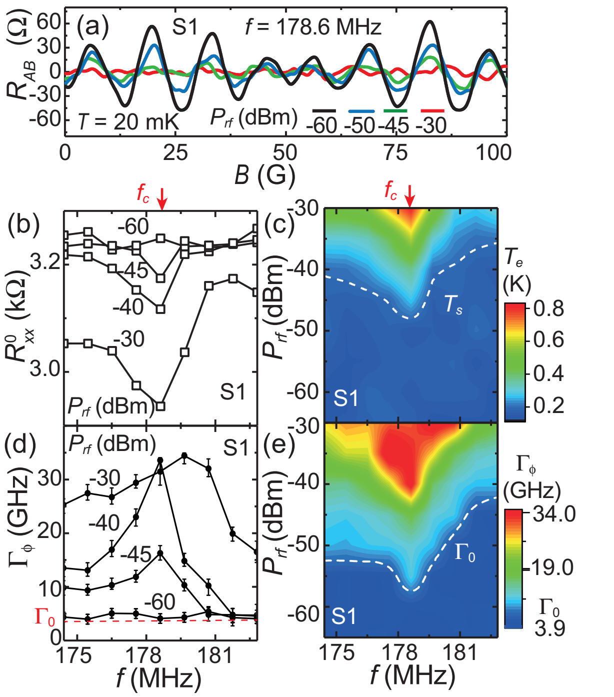

FIG. 2. (a) Representative data of the Aharonov-Bohm (AB) oscillations R_{AB} of S1 vs magnetic field B measured at $T = 20\,\mathrm{mK}$ under different P_{rf} applied on IDT1 at $f_c = 178.6\,\mathrm{MHz}$, while IDT2 is grounded. (b) Selected background traces of R^0_{xx} as a function of f at various P_{rf} applied on IDT1. (c) Interpolated color plot of the electron temperature T_e derived from R^0_{xx}, as a function f and P_{rf}. The white dashed line marks an isothermal line of saturation temperature T_s at 190 mK. (d) Decoherence rate Γ_ϕ vs f at different P_{rf}. Note that the error bar increases as P_{rf} rises. For clarity, only a few selected data are shown. (e) Interpolated color plot of the decoherence rate Γ_ϕ as a function of f and P_{rf}. The white dashed line indicates the borderline of Γ_0.

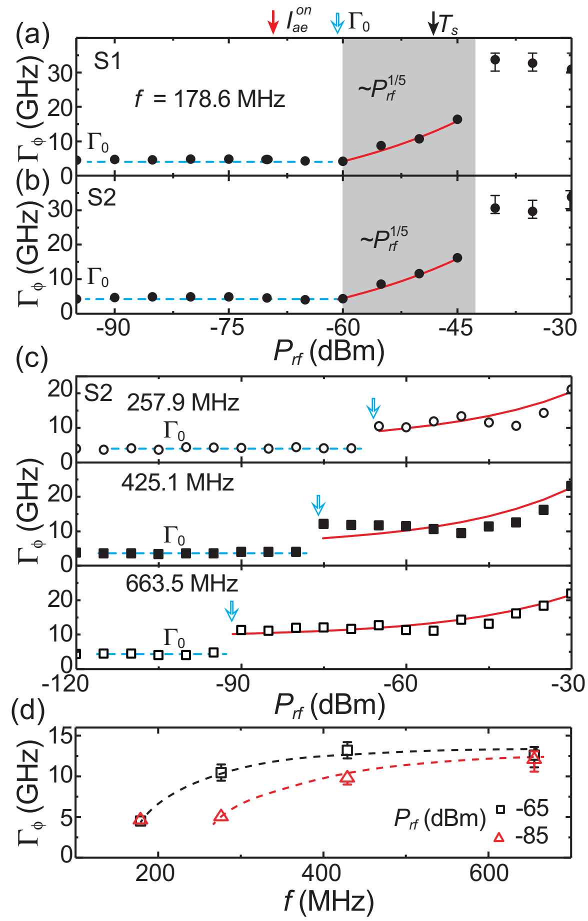

FIG. 3. The decoherence rate Γ_ϕ as a function of P_{rf} at $f_c = 178.6\,\mathrm{MHz}$ for (a) S1 and (b) S2. The dashed lines show that the decoherence rate Γ_ϕ saturates at Γ_0 when the radio-frequency (RF) power <-60 dBm, above which Γ_ϕ substantially increases. The hollow blue arrow marks the threshold P_{rf} of dephasing. In addition, the red and black arrows indicate the P_{rf} required for $I^{\mathrm{on}}_{\mathrm{ae}}$ and $T_e = T_s$, respectively. The red solid lines are the fitted power law $\Gamma_\phi \propto P_{\mathrm{rf}}^{1/5}$ at $f = f_c$ for S1 and S2. Note that only data within the shaded are used for fitting. (c) Traces of Γ_ϕ vs P_{rf} for S2 at $f \geqslant f_c$ for comparison. (d) Frequency dependence of Γ_ϕ for S2 at $P_{\mathrm{rf}} = -85$ and -65 dBm, respectively. The dashed lines are a guide to the eye to illustrate the increase of Γ_ϕ with increasing f.

thermal effects on dephasing become pronounced. For the red region shown in Fig. 2(e), $\Gamma_\phi \sim 32.5 \pm 2.5$ GHz, where the AB oscillation is no longer visible. We conclude that the electrons have completely lost their phase coherence, corresponding to T_e rising to $\sim$0.8 K. This temperature difference is $\sim$0.25 K lower than the maximum T ($\sim$1.05 K) observed in pure temperature dephasing measurements [see Fig. 1(e)], suggesting the existence of additional noise introduced by initiating the RF-EM field on IDT1. Furthermore, comparing the frequency dependence of $S_{21}(f)$ with that of $T_s(f)$ and $\Gamma_0(f)$, we find that their bandwidths are all $\sim$1.5 MHz. This consistence suggests that they are correlated with the Bragg reflection of SAW, as discussed earlier.

Figures 3(a) and 3(b) plot the decoherence rate Γ_ϕ vs P_{rf} of S1 and S2 at $f = f_c$, respectively. It appears that both traces show consistent behaviors. We mark the onset of RF power for discernible acoustoelectric current $I^{\mathrm{on}}_{\mathrm{ae}}$ observed at ~ -67 dBm, dephasing at ~ -60 dBm, and $T_e \geqslant T_s$ at ~ -48 dBm by the red, hollow blue, and black arrows, respectively, as indicated on the top axis. Notably, Γ_ϕ saturates at the value of Γ_0 under a weak SAW perturbation with $P_{\mathrm{rf}} < -60$ dBm. As RF power is in the range of -60 to -48 dBm, Γ_ϕ increases with P_{rf}, while T_e remains lower than T_s. It suggests that the thermal-related dephasing is negligible within this power range, and the applied RF-EM field plays a prominent role in decoherence. When $P_{\mathrm{rf}} > -48$ dBm, the heating effect becomes significant as $T_e \geqslant T_s$.

Altshuller *et al.* [9] predicted that high-frequency electric field-generated thermal fluctuations in disordered conductors can efficiently suppress the localization effect. Authors of later studies further suggested that the dephasing effect induced by the RF-EM field is far more devastating than heating [10,11]. Here, we denote the RF-EM field-induced decoherence rate as Γ_{ac} and consider the total decoherence rate as $\Gamma_\phi = \Gamma_0 + \Gamma_{\mathrm{ac}}$, where Γ_0 is the intrinsic decoherence rate with a characteristic frequency f_0. In Ref. [9], Altshuller *et al.* showed that Γ_ϕ increases with increasing f for $f < f_0$, reaches maximum at $f = f_0$, and decreases for $f > f_0$.

Additionally, they predicted $\Gamma_{ac} \propto P_{rf}^{1/5}$ in the limit of $\Gamma_\phi \sim \Gamma_{ac}$. More recently, in an experimental study on the AB oscillations in a normal-metal ring, Wenzler and Mohanty [12] confirmed the anticipated RF power dependence of Γ_ϕ when Γ_{ac} is larger than Γ_0.

Next, we explore the decoherence mechanism responsible for Γ_{ac} in our interferometer. The emergence of the $h/2e$ peak in Fig. 1(c), known as Altshuler-Aronov-Spivak oscillations, is associated with the weak localization of electrons [31,32], suggesting that conditions assumed in the theory proposed in Ref. [9] are applicable to our case. We investigate the power dependence of Γ_ϕ at $f_c = 178.6$ MHz for data limited in the shaded area shown in Figs. 3(a) and 3(b), where Γ_{ac} outweighs Γ_0 and $T_e \leqslant T_s$. The red lines are the fitted power law $\Gamma_\phi \propto P_{rf}^{1/(5\pm0.3)}$, in good agreement with theoretical predictions based on the consideration of the radiated EM field-induced thermal heating process in disordered conductors [9]. How the EM field-induced dephasing happens in a ballistic conductor requires more theoretical studies. Figure 3(c) shows the P_{rf} dependence of Γ_ϕ of S2 at three selected frequencies of 257.9, 425.1, and 663.5 MHz, which are chosen to be substantially above f_c and below f_0, where f_0 is the characteristic frequency defined as $f_0 = \Gamma_0$. We note that $f_0 \sim 3.9$ GHz. The blue arrows specify the threshold RF power above which $\Gamma_\phi \pi$ is considerably higher than Γ_0. Notably, this threshold power decreases with increasing frequency, suggesting that even a relatively weaker power level can cause phase breaking under a higher-frequency excitation. This trend is consistent with observations in the experiment of microwave-induced dephasing in one-dimensional metal wires [11]. As shown in Fig. 3(d), Γ_ϕ rises with increasing frequency under low RF power levels of -65 and -85 dBm, where the heating effect can be ignored. This feature is qualitatively consistent with theoretical predictions [31]. We stress that it is challenging to explore the frequency dependence of $\Gamma_\phi(f)$ for the full frequency range because the frequency bandwidth of the surrounding EM field of the interferometer is limited by the IDTs filter. The $P_{rf}^{1/5}$ dependence of Γ_ϕ at f_c shows effects can be quantitatively described by the theory in Ref. [9], which is based on the consideration of the radiation EM field-induced thermal heating process in disordered conductors.

To reveal more details of the effects of the SAW on the dephasing process, we examine the frequency dependence of I_{ae}. Figure 4(a) shows the acoustoelectric current I_{ae} vs f at various P_{rf} for S1 at $T = 20$ mK in the absence of a magnetic field. Figure 4(b) presents a color plot of $I_{ae}(f, P_{rf})$, where the white dashed line with an asymmetric frequency dependence, also observed in T_e and Γ_ϕ, indicates the isovalue line of I_{ae}^{on}. The bandwidth of $I_{ae}^{on}(f)$ is $\sim$1.5 MHz, consistent with the bandwidth of $S_{21}(f)$ originating from SAW reflections. This suggests that the piezoelectric field is the dominant component of the EM field in decoherence at f_c under a weak RF drive. The asymmetric feature becomes more pronounced as P_{rf} increases, as shown in Fig. 4(a). The observed asymmetry in I_{ae}^{on} is in qualitative agreement with the crosstalk effect from the stray RF fields induced by the metallic transducers, which introduces a declining background level when frequency moves away from f_c [33]. Therefore, the influence of the crosstalk of the SAW on the I_{ae} spectrum accounts for the asymmetric spectra of T_e and Γ_ϕ observed in Figs. 2(c) and 2(e), respectively. Moreover, it is interesting to note that I_{ae} does not exhibit the AB oscillations, likely due to the significant attenuation of SAWs arising from intriguing interaction with 2DEG.

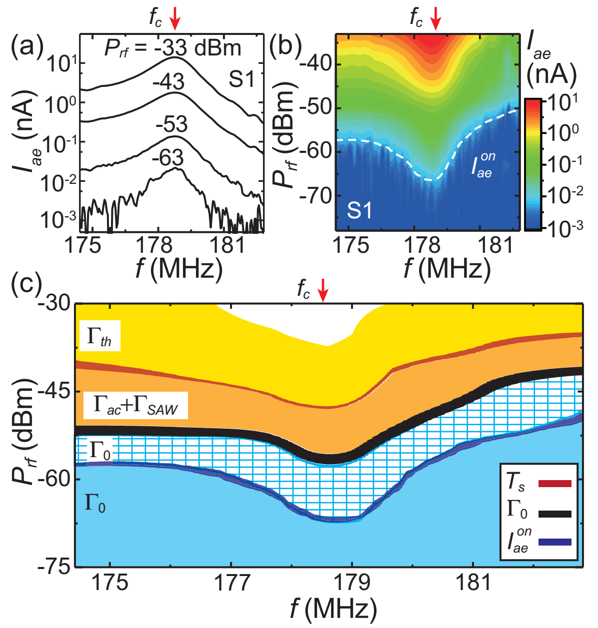

FIG. 4. (a) Frequency dependence of the acoustoelectric current I_{ae} for S1 around f_c under various P_{rf} at zero magnetic field, measured at $T = 20$ mK. I_{ae} exhibits an asymmetric frequency dependence with a maximum at f_c, indicating the presence of an f-dependent background arising from crosstalk. For a numerical comparison with the P value, the magnitude of radio-frequency (RF) power under pulse modulation has been calibrated to be comparable with that under a continuous drive. (b) Color plot of I_{ae} as a function of f and P_{rf}. The white dashed line displays the accessible (f, P_{rf}) for I_{ae}^{on}. (c) The integrated P_{rf}-f plot of the isovalue lines of T_s, Γ_0, and I_{ae}^{on}, obtained from Figs. 2(c), 2(e) and 4(b), respectively. The dephasing process in each zone separated by the isovalue lines is dominated by a specific interplay of decoherence sources.

The SAW-induced I_{ae} ranges from $\sim$10 pA to 10 nA, depending on the applied SAW excitation power. At the maximum SAW power of ~ -30 dBm, I_{ae} is comparable with the AC excitation I_{SD} used in the lock-in measurements. At low temperatures and under low SAW RF power < -60 dBm, clear AB interference patterns are observed, indicating that the current amplitude is small enough to preserve the interference patterns. We estimate the AC electric voltage across the AB ring to have an order of magnitude of 30 μV, which is too small to modulate the AB phase by altering the electron trajectories within the ring and, consequently, its area. Even at the highest SAW power of -30 dBm in our experiment, the modulation voltage, as referenced from Ref. [26], is <1.0 mV, which is one to two orders of magnitude smaller than the typical gate voltage of ~ -0.1 V observed in GaAs interferometers [7] and significantly lower than the threshold voltage required to suppress AB interference [6].

Figure 4(c) summarizes the isovalue lines of T_s, Γ_0, and I_{ae}^{on} as a function of f and P_{rf} obtained from Figs. 2(c), 2(e) and 4(b), respectively. Notably, there is no crossover between any two isovalue lines, suggesting a superimposed-oriented phase-breaking process. This map allows us to investigate the evolution of Γ_ϕ with the emergence of different dephasing sources. Under a weak RF drive ($P_{rf} \leqslant -67$ dBm), Γ_ϕ retains at Γ_0, marked by the blue zone, where T_e stays at the base temperature. As the RF power increases and enters the blue square-hatching zone bounded by the isovalue line of I_{ae}^{on} and Γ_0, Γ_ϕ remains unchanged even in the presence of SAW. Our finding has an implication for shuttling electrons by manipulating the SAW technique. The acoustoelectric current can be expressed as $I_{ae} = nef$, where n is the number of transferred electrons per SAW cycle. Based on the value of I_{ae} appearing in the blue square-hatching zone, we can estimate n to be ~2 electrons without experiencing phase breaking, even under a continuous drive. Consequently, this zone is identified as an optimal condition for operating flying-qubit devices.

We now consider the spectra of the obtained $S_{21}(f)$ and $I_{ae}(f)$, which correspond to the EM field spectrum $S_{ac}(f)$ and the SAW spectrum $S_{SAW}(f)$, respectively. We express the total decoherence rate Γ_ϕ as the sum of its individual components: $\Gamma_\phi = \Gamma_{th} + \Gamma_{ac} + \Gamma_{SAW}$, representing the temperature-, EM field-, and SAW-correlated decoherence rate, respectively. Here, Γ_{ac} originates from the alternating current driven by the piezoelectric field, and Γ_{SAW} is related to the fluctuations and attenuation of the piezoelectric potential associated with the SAW propagation, while the I_{ae}-lacking AB phase is attributed to the attenuation of SAWs interacting with 2DEG.

The interplay between Γ_{ac} and Γ_{SAW} becomes pronounced in the orange zone, where $P_{rf} \geqslant -57$ dBm. Our data analysis indicates that Γ_{ac} and Γ_{SAW} are two major phase-breaking sources when $T_e \leqslant T_s$, both originating from piezoelectric effect. We estimate $\Delta\Gamma_{ac} + \Delta\Gamma_{SAW}$~6.6 GHz for -57 dBm $\leqslant P_{rf} \leqslant -48$ dBm around f_c. This finding provides evidence that the piezoelectric field noise-induced dephasing is present in the orange zone without a concomitant overheating of the electrons. We wish to address another essential but unsettled issue at this point. Earlier experimenters reported that the flying qubit could be more robust against the fluctuations of an impurity potential when a SAW is operated at a higher frequency [34]. However, as far as the phase coherence is concerned, considering the phase coherence, our results suggest that the optimal frequency for SAW operation is upper limited by f_0 due to the effect of Γ_{ac}.

We cannot distinguish the effect of Γ_{SAW} from Γ_ϕ for frequency around f_c in the orange zone. However, by analyzing the asymmetry of Γ_ϕ under off-resonance conditions, we can estimate the value of Γ_{SAW}; for example, $\Delta\Gamma_{SAW}$~5.3 GHz by taking the difference of Γ_ϕ at $f_c \pm 4.2$ MHz and $P_{rf} = -41.5$ dBm. As we go across the isovalue line of T_s and get into the yellow zone where the thermal heating effects emerge, the roles of Γ_{th}, Γ_{SAW}, and Γ_{ac} in phase breaking are intertwined, making it experimentally challenging to distinguish among them. While $P_{rf} \geqslant -40$ dBm, the coherence of the AB phase is no longer sustained, indicating total dephasing, i.e., $\Gamma_\phi \geqslant 29$ GHz, marked by the white zone.

Finally, we wish to discuss the underlying decoherence mechanisms in our experiments. The dissipative effects

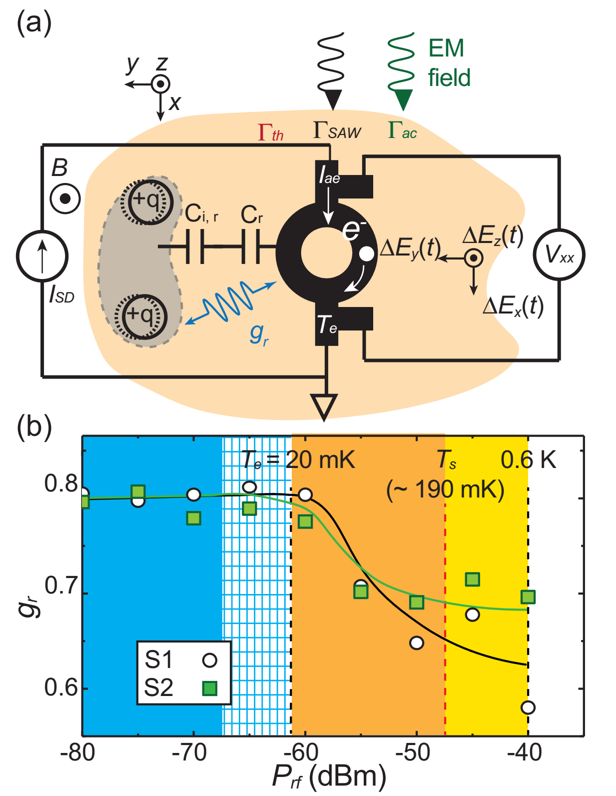

FIG. 5. (a) Pictorial diagram to illustrate the interplay of various noise sources with the charge fluctuations between the impurities ($+q$) and electrons in the ring path, which carry the Aharonov-Bohm (AB) phase information. The external noises include the environmental thermal noise characterized by Γ_{th}, radio-frequency (RF)-electromagnetic (EM) field noise represented by Γ_{ac}, noise from the surface acoustic wave (SAW) signified by Γ_{SAW}, and internal I_{ae} flowing along the ring. The parameter g_r represents the coupling strength of e-e interactions between the charged impurities and the electrons residing in the arm. Each arm of the ring is coupled to the impurities via a geometric capacitance C_r and an equivalent quantum capacitance $C_{i,r}$, defined as $e^2 D_i$, where D_i is the impurity density of states. (b) g_r as a function of P_{rf}. The value of g_r is deduced from the RF power dependence of Γ_ϕ. The black and green solid lines are guides to the eye.

during the AB phase accumulation govern the decoherence of an AB interferometer. As a result, the interferometer is sensitive to the potential fluctuations along the trajectory of electrons in the ring. Here, we adopt the theory developed by Seelig and Büttiker [4], confirmed by numerous studies [6–8,35], to describe a dephasing process depicted in Fig. 5(a). The schematic diagram illustrates the four-terminal AB ring threaded by a magnetic flux, in the presence of a thermal background, and subjected to an RF-EM field and SAW. Each arm of the ring is coupled to its surrounding charged impurities ($+q$) by a coupling parameter g_r (dimensionless Luttinger parameter). This dimensionless parameter gives an effective measure of the strength of the interaction between the electrons, with $g_r \to 1$ corresponding to a noninteracting case. The external perturbations, characterized by the decoherence rate Γ_ϕ, cause charge fluctuations in the arms of the ring, leading to the effective internal potential fluctuations ΔU.

As a result, electrons moving along the ring path experience these potential fluctuations and lose phase coherence after undergoing an inelastic scattering.

In the absence of an RF-EM field and SAW, the decoherence rate can be expressed as

$$\Gamma_\phi = \Gamma_{\rm th} = \left(\frac{\pi}{3}\right)\frac{k_B T}{\hbar}\left(1 - g_r^2\right)^2. \quad (2)$$

Equation (2) can be rewritten as $\Gamma_\phi = (\frac{2e^2}{3\hbar^2})(\frac{C_{\mu,r}}{C_r})^2 k_B T R_q$, where R_q represents the charge relaxation resistance, $C_{\mu,r}$ is the electrochemical capacitance, and C_r is the geometric capacitance of the ring. Note that $C_{\mu,r}^{-1} = C_r^{-1} + C_{i,r}^{-1}$, where $C_{i,r} = e^2 D_i$ is an equivalent quantum capacitance, and D_i is the impurity density of states [4]. The ratio $\frac{C_{\mu,r}}{C_r}$, defined as $(1 - g_r^2)$, was previously considered a temperature-independent constant. Based on the linear temperature fit of Γ_ϕ shown in Fig. 1(e), we can evaluate $\frac{C_{\mu,r}}{C_r}\sim 0.4$ or $g_r\sim 0.8$, where $R_q\sim 3.4\,{\rm k}\Omega$, in fair agreement with previous studies [4,35].

Subsequently, we adopt Eq. (2) to analyze the $P_{\rm rf}$ dependence of Γ_ϕ. Note that Eq. (2) fails to explain the phase saturation below T_s. Strictly speaking, Eq. (2) is applicable to the conditions where $T_e > T_s$. Experimentally, it has been found that T_s spans a broad transition temperature range of $\sim$100 mK, which provides room to scrutinize the interplay of different phase-breaking processes. Figure 5(a) illustrates the high-frequency electric field $\vec{E}$ surrounding the ring and the charged impurity- induced electron-electron (*e*-*e*) interactions under the fluctuations of $\vec{E}$. In our device configuration, the electrons carrying the AB phase move along the x direction. The plane SAW induced by IDT1 generates a piezoelectric field $\vec{E}$ with two components, E_x and E_z, propagating parallel and perpendicular to the electron trajectory, respectively. These electric field components are associated with what is known as the Rayleigh mode, the longitudinal and shear SAWs (for details, see Chapter 1 in Ref. [36]). Furthermore, the interdigital capacitance of IDT behaves as an on-chip wideband antenna, radiating an EM field that contributes to $\vec{E}$ [37].

In general, the EM phase of the electrons traveling along the arm of the ring can be expressed as

$$\varphi = (k_F + \Delta k)L + \left(\frac{e}{\hbar}\right)\left[\int V(t)dt + \int \vec{A}\cdot d\vec{r}\right]. \quad (3)$$

Here, the length L of each arm is equal, k_F is the Fermi wave vector, Δk is the fluctuation of the wave vector induced by ΔU, and the last two terms account for the phase shift caused by the electrostatic and vector potentials V and $\vec{A}$ in the low-frequency limit, respectively. Equation (2) was derived [5] mainly by considering the second term in Eq. (3). Here, V in the second term includes static electric potential and longitudinal fluctuating electric potential, and $\vec{A}$ in the third term contains static vector potential and dynamical fluctuating vector potential, giving rise to fluctuating magnetic fields together with the transverse fluctuating electric fields [38]. Experimental studies on the electrostatic AB effect in the presence of E_x [39,40] and E_y [41] have been reported. In addition, it has been shown that the presence of E_z alters the confining potential of the ring and the resident carrier density [42,43]. Either of them could cause the potential deformation and, in turn, generate Δk [4].

With an understanding of the roles of each component of $\vec{E}$ in the EM phase, we now consider that the fluctuations of $\vec{E}(t)$ can effectively modulate the strength of the charge fluctuation and the *e*-*e* interaction. These effects can be conceptually cast into the parameter g_r in the Ref. [4] approach, as illustrated in Fig. 5(a). We extract g_r based on data shown in Figs. 3(a) and 3(b) and plot it as a function of $P_{\rm rf}$ for S1 and S2 in Fig. 5(b). The g_r value decreases from 0.8 to 0.6 with increasing $P_{\rm rf}$, suggesting that the *e*-*e* interaction is enhanced with increasing RF power. The decrease of g_r implies a reduction in the screening effect, which thus enhances the electron-electron collision rate and heats up the electronic temperature, in analogy with the results discussed in Ref. [9]. Further exploration of the role of the EM field and SAW would require a better understanding of the detailed phase-breaking processes. To fully account for the effects of the EM field and SAW, one has to put more sophisticated interactions in theoretical considerations, for example, the low-frequency absorption of the EM waves and the influence of Doppler effects on k_F of electrons due to currents generated by SAW. Our experimental work highlights the complexity of these processes and can stimulate future theoretical studies to explore the intricate phase-breaking mechanism induced by the thermal effects of the EM field and SAW in a ballistic quantum transport system.

III. CONCLUSIONS

In conclusion, we have measured the frequency and power dependence of the AB oscillations in a ballistic quantum interferometer made on the piezoelectric substrate GaAs/AlGaAs heterostructure with a 2DEG, under the influences of the SAW and RF-EM field, which specifically refers to the piezoelectric field, both generated by a local IDT. We obtain the RF power dependence of the spectrum of decoherence rate Γ_ϕ, electronic temperature T_e, and acoustoelectric current $I_{\rm ae}$ to highlight the relevant phase-breaking processes at various RF power levels. We find that the EM field-induced decoherence rate without thermal heating follows $\Gamma_\phi \propto P_{\rm rf}^{1/5}$ and unveil that the piezoelectric component of the EM field is primarily responsible for the decoherence process. Furthermore, we determine the operational conditions for the SAW to retain the charge coherence. By extracting the SAW-correlated $\Gamma_{\rm SAW}$ from the asymmetric Γ_ϕ spectrum, we examine the heating effects induced by high-power RF drives. Finally, we attribute the observed decoherence to the intricate interplay between the charged impurity-correlated *e*-*e* interactions and the presence of the SAW and RF-EM field. More theoretical investigations are needed to further elucidate the observed phase-breaking processes.

ACKNOWLEDGMENTS

We acknowledge Shi-Xuan Hong for his experimental assistance. J.C.C. acknowledges financial support from the National Science and Technology Council of Taiwan under Projects No. 110-2112-M-007-022-MY3 and No. 111-2119-

M-007-008. We also acknowledge support from the Center for Quantum Science and Technology within the framework of the Higher Education Sprout Project by the Ministry of Education, Taiwan.

[1] Y. Makhlin, G. Schön, and A. Shnirman, Quantum-state engineering with Josephson-junction devices, Rev. Mod. Phys. **73**, 357 (2001).

[2] A. A. Clerk, M. H. Devoret, S. M. Girvin, F. Marquardt, and R. J. Schoelkopf, Introduction to quantum noise, measurement, and amplification, Rev. Mod. Phys. **82**, 1155 (2010).

[3] G. Burkard, T. D. Ladd, A. Pan, J. M. Nichol, and J. R. Petta, Semiconductor spin qubits, Rev. Mod. Phys. **95**, 025003 (2023).

[4] G. Seelig and M. Büttiker, Charge-fluctuation-induced dephasing in a gated mesoscopic interferometer, Phys. Rev. B **64**, 245313 (2001).

[5] M. Büttiker and A. M. Martin, Charge relaxation and dephasing in Coulomb-coupled conductors, Phys. Rev. B **61**, 2737 (2000).

[6] K. T. Lin, Y. Lin, C. C. Chi, J. C. Chen, T. Ueda, and S. Komiyama, Temperature- and current-dependent dephasing in an Aharonov-Bohm ring, Phys. Rev. B **81**, 035312 (2010).

[7] K. T. Lin, Y. Lin, C. C. Chi, and J. C. Chen, Asymmetric transmission-induced probe-configuration-dependent dephasing in an Aharonov-Bohm ring, Phys. Rev. B **84**, 235404 (2011).

[8] A. E. Hansen, A. Kristensen, S. Pedersen, C. B. Sørensen, and P. E. Lindelof, Mesoscopic decoherence in Aharonov-Bohm rings, Phys. Rev. B **64**, 045327 (2001).

[9] B. Altshuller, A. Aronov, and D. Khmelnitsky, Suppression of localization effects by the high frequency field and the Nyquist noise, Solid State Commun. **39**, 619 (1981).

[10] B. Altshuler, M. Gershenson, and I. Aleiner, Phase relaxation of electrons in disordered conductors, Physica E **3**, 58 (1998).

[11] J. Wei, S. Pereverzev, and M. E. Gershenson, Microwave-induced dephasing in one-dimensional metal wires, Phys. Rev. Lett. **96**, 086801 (2006).

[12] J.-S. Wenzler and P. Mohanty, Measurement of Aharonov-Bohm oscillations in mesoscopic metallic rings in the presence of a high-frequency electromagnetic field, Phys. Rev. B **77**, 121102(R) (2008).

[13] C. Bäuerle, D. C. Glattli, T. Meunier, F. Portier, P. Roche, P. Roulleau, S. Takada, and X. Waintal, Coherent control of single electrons: A review of current progress, Rep. Prog. Phys. **81**, 056503 (2018).

[14] M. V. Gustafsson, T. Aref, A. F. Kockum, M. K. Ekström, G. Johansson, and P. Delsing, Propagating phonons coupled to an artificial atom, Science **346**, 207 (2014).

[15] M. Kataoka, M. R. Astley, A. L. Thorn, D. K. L. Oi, C. H. W. Barnes, C. J. B. Ford, D. Anderson, G. A. C. Jones, I. Farrer, D. A. Ritchie *et al.*, Coherent time evolution of a single-electron wave function, Phys. Rev. Lett. **102**, 156801 (2009).

[16] S. Hermelin, S. Takada, M. Yamamoto, S. Tarucha, A. D. Wieck, L. Saminadayar, C. Bäuerle, and T. Meunier, Electrons surfing on a sound wave as a platform for quantum optics with flying electrons, Nature (London) **477**, 435 (2011).

[17] R. P. G. McNeil, M. Kataoka, C. J. B. Ford, C. H. W. Barnes, D. Anderson, G. A. C. Jones, I. Farrer, and D. A. Ritchie, On-demand single-electron transfer between distant quantum dots, Nature (London) **477**, 439 (2011).

[18] J. Dubois, T. Jullien, F. Portier, P. Roche, A. Cavanna, Y. Jin, W. Wegscheider, P. Roulleau, and D. C. Glattli, Minimal-excitation states for electron quantum optics using levitons, Nature (London) **502**, 659 (2013).

[19] B. Bertrand, S. Hermelin, S. Takada, M. Yamamoto, S. Tarucha, A. Ludwig, A. D. Wieck, C. Bäuerle, and T. Meunier, Fast spin information transfer between distant quantum dots using individual electrons, Nat. Nanotechnol. **11**, 672 (2016).

[20] S. Takada, H. Edlbauer, H. V. Lepage, J. Wang, P.-A. Mortemousque, G. Georgiou, C. H. Barnes, C. J. Ford, M. Yuan, P. V. Santos *et al.*, Sound-driven single-electron transfer in a circuit of coupled quantum rails, Nat. Commun. **10**, 4557 (2019).

[21] J. Wang, H. Edlbauer, A. Richard, S. Ota, W. Park, J. Shim, A. Ludwig, A. D. Wieck, H.-S. Sim, M. Urdampilleta *et al.*, Coulomb-mediated antibunching of an electron pair surfing on sound, Nat. Nanotechnol. **18**, 721 (2023).

[22] P. Mohanty, E. M. Q. Jariwala, and R. A. Webb, Intrinsic decoherence in mesoscopic systems, Phys. Rev. Lett. **78**, 3366 (1997).

[23] J. J. Lin and J. P. Bird, Recent experimental studies of electron dephasing in metal and semiconductor mesoscopic structures, J. Phys. Condens. **14**, R501 (2002).

[24] T. J. Thornton, M. Pepper, H. Ahmed, D. Andrews, and G. J. Davies, One-dimensional conduction in the 2D electron gas of a GaAs-AlGaAs heterojunction, Phys. Rev. Lett. **56**, 1198 (1986).

[25] T. J. Thornton, M. L. Roukes, A. Scherer, and B. P. Van de Gaag, Boundary scattering in quantum wires, Phys. Rev. Lett. **63**, 2128 (1989).

[26] R. J. Schneble, M. Kataoka, C. J. B. Ford, C. H. W. Barnes, D. Anderson, G. A. C. Jones, I. Farrer, D. A. Ritchie, and M. Pepper, Quantum-dot thermometry of electron heating by surface acoustic waves, Appl. Phys. Lett. **89**, 122104 (2006).

[27] P. Utko, P. E. Lindelof, and K. Gloos, Heating in single-electron pumps driven by surface acoustic waves, Appl. Phys. Lett. **88**, 202113 (2006).

[28] J. de Lima, M. M., F. Alsina, W. Seidel, and P. V. Santos, Focusing of surface-acoustic-wave fields on (100) GaAs surfaces, J. Appl. Phys. **94**, 7848 (2003).

[29] D. Morgan, *Surface Acoustic Wave Filters: With Applications to Electronic Communications and Signal Processing* (Academic Press, Oxford, 2010).

[30] J. M. Shilton, V. I. Talyanskii, M. Pepper, D. A. Ritchie, J. E. F. Frost, C. J. B. Ford, C. G. Smith, and G. A. C. Jones, High-frequency single-electron transport in a quasi-one-dimensional GaAs channel induced by surface acoustic waves, J. Phys. Condens. **8**, L531 (1996).

[31] B. L. Al'tshuler, A. G. Aronov, and B. Z. Spivak, The Aaronov-Bohm effect in disordered conductors, Sov. Phys. JETP Lett. **33**, 101 (1981).

[32] D. Y. Sharvin and Y. V. Sharvin, Magnetic-flux quantization in a cylindrical film of a normal metal, Sov. Phys. JETP Lett. **34**, 285 (1981).

[33] J. M. Shilton, D. R. Mace, V. I. Talyanskii, M. Pepper, M. Y. Simmons, A. C. Churchill, and D. A. Ritchie, Effect of spatial dispersion on acoustoelectric current in a high-mobility two-dimensional electron gas, Phys. Rev. B **51**, 14770 (1995).

[34] V. Talyanskii, J. Shilton, J. Cunningham, M. Pepper, C. Ford, C. Smith, E. Linfield, D. Ritchie, and G. Jones, Quantized current in one-dimensional channel induced by surface acoustic waves, Phys. B: Condens. Matter **249-251**, 140 (1998).

[35] T. S. Lo, Y. P. Lin, P. M. Wu, D. C. Ling, C. C. Chi, and J. C. Chen, Mode dependency of quantum decoherence studied via an Aharonov-Bohm interferometer, Phys. Rev. Lett. **116**, 080401 (2016).

[36] C. K. Campbell, *Surface Acoustic Wave Devices for Mobile and Wireless Communications, Four-Volume Set* (Academic Press, San Diego, 1998).

[37] G. Alley, Interdigital capacitors and their application to lumped-element microwave integrated circuits, IEEE Trans. Microw. Theory Tech. **18**, 1028 (1970).

[38] A. Walstad, A critical reexamination of the electrostatic Aharonov-Bohm effect, Int. J. Theor. Phys. **49**, 2929 (2010).

[39] A. van Oudenaarden, M. H. Devoret, Y. V. Nazarov, and J. E. Mooij, Magneto-electric Aharonov–Bohm effect in metal rings, Nature (London) **391**, 768 (1998).

[40] W. G. van der Wiel, Y. V. Nazarov, S. De Franceschi, T. Fujisawa, J. M. Elzerman, E. W. G. M. Huizeling, S. Tarucha, and L. P. Kouwenhoven, Electromagnetic Aharonov-Bohm effect in a two-dimensional electron gas ring, Phys. Rev. B **67**, 033307 (2003).

[41] P. G. N. de Vegvar, G. Timp, P. M. Mankiewich, R. Behringer, and J. Cunningham, Tunable Aharonov-Bohm effect in an electron interferometer, Phys. Rev. B **40**, 3491 (1989).

[42] C. Ford, A. Fowler, J. Hong, C. Knoedler, S. Laux, J. Wainer, and S. Washburn, Gated, asymmetric rings as tunable electron interferometers, Surf. Sci. **229**, 307 (1990).

[43] S. S. Buchholz, S. F. Fischer, U. Kunze, M. Bell, D. Reuter, and A. D. Wieck, Control of the transmission phase in an asymmetric four-terminal Aharonov-Bohm interferometer, Phys. Rev. B **82**, 045432 (2010).